Hydrodynamically-enhanced transfer of dense non-aqueous phase liquids into an aqueous reservoir

Nadia Valletti [a,1], Marcello A. Budroni [b,1], Paola Albanese [a], Nadia Marchettini [a], Margarita Sanchez-Dominguez [c], Istvan Lagzi [d,e], Federico Rossi [a,*]

[a] *Department of Earth, Environmental and Physical Sciences, University of Siena, Pian dei Mantellini 44, 53100 Siena, Italy*
[b] *Department of Chemical, Physical, Mathematical and Natural Sciences, University of Sassari, Via Vienna 2, 07100 Sassari, Italy*
[c] *Grupo de Quimica Coloidal e Interfacial Aplicada a Nanomateriales y Formulaciones, Centro de Investigacion en Materiales Avanzados, S.C. (CIMAV), Unidad Monterrey, Alianza Norte 202, Parque de Investigacion e Innovacion Tecnologica, Apodaca 66628, Mexico*
[d] *Department of Physics, Institute of Physics, Budapest University of Technology and Economics, Muegyetem rkp. 3., H-1111 Budapest, Hungary*
[e] *ELKH-BME Condensed Matter Research Group, Budapest University of Technology and Economics, Muegyetem rkp. 3., H-1111 Budapest, Hungary*

ARTICLE INFO

ABSTRACT

The use of surfactants represents a viable strategy to boost the removal yield of Dense Non-Aqueous Phase Liquids (DNAPLs) from groundwater and to shorten the operational timing of the remediation process. Surfactants, in general, help in reducing the interfacial tension at the DNAPL/water interface and enhance the solubility of the pollutant in the water phase through the formation of dispersed systems, such as micelles and emulsions. In this paper, we show that a suitable choice of a surfactant, in this case belonging to the bio-degradable class of ethoxylated alcohols, allows for the formation of hydrodynamic interfacial instabilities that further enhances the dissolution rate of the organic pollutant into the water phase. In a stratified configuration (denser organic phase at the bottom and lighter water phase on top), the instabilities appear as upward-pointing fingers that originate from the inversion of the local density at the interface. This inversion stems from the synergetic coupling of two effects promoted by the ethoxylated surfactant: *i*) the enhanced co-solubility of the DNAPL into the water (and *viceversa*), and (*ii*) the differential diffusion of the DNAPL and the surfactant in the aqueous phase. By dissolving into the DNAPL, the surfactant also reduces locally the surface tension at the liquid–liquid interface, thereby inducing transversal Marangoni flows. In our work, we carefully evaluated the effects of the concentration of different surfactants (two different ethoxylated alcohols, sodium dodecylsulphate, cetyltrimethyl ammonium bromide, N-tetradecyl-N, N-dimethylamine oxide and bis(2-ethylhexyl) sulfosuccinate sodium salt) on the onset of the instabilities in 3 different DNAPLs/water stratifications, namely chloroform, trichloroethylene and tetrachloroethylene, with a special emphasis on the trichloroethylene/water system. By means of a theoretical model and nonlinear simulations, supported by surface tension, density and diffusivity measurements, we could provide a solid explanation to the observed phenomena and we found that the type of the dispersed system, the solubility of the DNAPL into the water phase, the solubility of the surfactant in the organic phase, as well as the relative diffusion and density of the surfactant and the DNAPL in the aqueous phase, are all key parameters for the onset of the instabilities. These results can be exploited in the most common remediation techniques.

1. Introduction

The remediation of sites polluted by Dense Non-Aqueous Phase Liquids (DNAPLs) poses several technological and environmental challenges. Most DNAPLs are chemically inert and recalcitrant to biological attacks, thus *in-situ* transformation or mineralisation is not easily achievable (Moccia et al., 2017; Hussain et al., 2022). For

these reasons, the most important remediation strategies rely on the removal of DNAPLs from the polluted site and their *ex-situ* chemical destruction by means of thermal incineration, heterogeneous catalytic mineralisation and advanced redox processes (Cucciniello et al., 2017; Intiso et al., 2019; Ebrahimbabaie and Pichtel, 2021; Hussain et al., 2022). However, even the removal itself is a demanding task; for example, due to the scarce solubility of the DNAPLs in water and

---

their high density, the classic pump and treat (P&T) technique is not quite effective. To partially overcome the mobility issues of the DNAPLs, P&T has been improved by adding surfactants, solvents and co-solvents to the injected water phase (*enhanced remediation* or *co-solvent/surfactant flushing*) (Huo et al., 2020). The presence of surfactants, in fact, lowers the interfacial tension between the DNAPLs and the aqueous phase and improves the solubility of the organic compounds in water, when the concentration of the surfactant is above the Critical Micellar Concentration (CMC).

Many amphiphilic molecules have been tested in terms of the molar solubilisation ratio (MSR) and a wide range of alternatives is nowadays available for their employment in remediation processes. However, the use of surfactants poses new problematics somehow overlooked in the past and related with their partitioning in the organic phase (Zimmerman et al., 1999), such as their potential harmfulness in case of accidental release and the risk of causing a downward mobilisation of DNAPLs (Ramsburg and Pennell, 2002). To mitigate these drawbacks, biodegradable surfactants can be harnessed and additional compounds added to the extracting solution thus modulating the density of the DNAPLs (Kibbey et al., 2002; Ramsburg and Pennell, 2002; Yang et al., 2022). Recently, we found that biodegradable ethoxylated alcohols belonging to the Synperonic™ family are effective for increasing the solubility of TCE in water (Intiso et al., 2018; Garza-Arévalo et al., 2019) and for accelerating the mass transfer during the dissolution processes (Valletti et al., 2021).

In this paper, we report the effect of two nonionic surface-active ethoxylated alcohols (Synperonic™ 91/10 and Synperonic™ 91/5) in initially stable stratifications, where they are employed in aqueous solutions layered on top of different DNAPL (chloroform, trichloroethylene and perchloroethylene). In particular their properties as solubility and density modulators were investigated. The presence of the surfactant in the less dense water phase at concentrations above 1×10^{-2} M, promoted the onset of hydrodynamic instabilities in the form of upwards plumes, that enhance the mixing of the two phases and, in particular, the DNAPL dissolution. We conducted our experiments in a Hele-shaw cell, which represents a viable model for porous media (Saffman and Taylor, 1958; Trevelyan et al., 2011), and we compared the results with surfactants belonging to other classes (anionic, cationic and zwitterionic). In our interpretation, instabilities stemmed from the inversion of the local density at the interface, due to the mutual solubilisation of the DNAPL in the upper aqueous phase and the surfactant in the bottom DNAPL, combined to their differential diffusion in the aqueous phase.

Several model systems have been developed to explore the behaviour of DNAPLs in subsurface, both to understand how the DNAPLs migrate into the soil or in the groundwater following a spillover, and/or to characterise the mobilisation of the DNAPLs during the remediation procedures (Agaoglu et al., 2015; Engelmann et al., 2019). In general, these multiphase flow models aim to predict the mass transfer of DNAPLs in aqueous solutions as a function of the boundary and environmental conditions (porosity, temperature etc.) and the most influential parameters were found to be the flow velocity and the contact time between different phases. In the case of remediation applications, the lowering of the surface tension and the enhancement of the DNAPL solubility, due to the presence of surfactants, also play a fundamental role. Most of the experimental models were devised in pseudo 2-dimensional tank reactors where the mass transfer of the DNAPLs to the water compartments was characterised as a function of the environmental conditions and of the relative flow-rate of the liquids (Luciano et al., 2010, 2012, 2018; Liu et al., 2014; Colombano et al., 2021; Wang et al., 2022).

However, in this work we did not consider the transversal flow of the water phase at the interface; rather, we were interested in understanding the spontaneous onset of the instabilities in static conditions. Therefore, we adopted a slightly different modelling approach and we framed the problem in the context of the convective dissolution between partially miscible or immiscible fluids. This aspect has been thoroughly investigated due to its relevance for many applied processes, ranging from petroleum recovery and CO_2 geologic sequestration to materials and pharmaceutical engineering. The generation and control of convective flows in such systems is of practical importance because hydrodynamics can sustain a mass transfer from one fluid phase to the other much more intensively than molecular diffusion. The theoretical models developed and optimised in this context rely on the general Navier–Stokes equations (or related formulation like Darcy's equations) coupled to Fickian diffusion and to chemical terms, if any reaction is at play (Lappa et al., 2005; Bratsun and De Wit, 2004; Budroni et al., 2014; Loodts et al., 2014; De Wit, 2016; Budroni et al., 2017). Here we adopted this general framework which, supported by experimental measurements of the fluid densities and species diffusivities, could provide a solid description and an explanation of the dynamics observed.

2. Materials and methods

2.1. Chemicals

Synperonic™ 91/5 (Syn 91/5, Polyoxyethylene(5) C9-C11 alcohol, density 0.978 g cm^{-3}) and Synperonic™ 91/10 (Syn 91/10, Polyoxyethylene(10) C9-C11 alcohol, density 0.998 g cm^{-3}) are biodegradable ethoxylated alcohols, provided by Croda International (UK). Synperonic™ solutions at different concentrations were prepared by dilution from a stock solution having a concentration 1.00 M. The anionic surfactant bis(2-ethylhexyl) sulfosuccinate sodium salt (AOT, 95% purity) was purchased from Sigma-Aldrich (St. Louis, MO, USA). The cationic surfactant cetyltrimethylammonium bromide (CTAB 99% purity) was purchased from Acros Organic (New Jersey, USA). The zwitterionic *N*-tetradecyl-*N,N*-dimethylamine (C14-DMAO) was a gift of Prof. H. Hoffman (Bayreuth Center for Colloids & Interfaces). The anionic surfactant sodium dodecyl sulfate (SDS 99% purity) was purchased from BIOCHEM Chemopharma (Cosne sur loire, France). The relevant properties of surfactants are given in Table 1 and the chemical structures are reported in Fig. 1(a). Surfactant solutions were prepared according to their solubility in water. In particular, AOT was used in the concentration range 0.01 M – 0.05 M, CTAB in the range 0.01 M – 0.03 M, C14-DMAO in the range 0.05 M – 0.10 M and SDS in the range 0.10 M – 1.00 M.

Three chlorinated organic compounds, trichloroethylene (TCE), tetrachloroethylene (PCE) and chloroform (CF) were used as representatives of the DNAPLs group. TCE (analytical grade > 99.5%) was purchased from Sigma-Aldrich (St. Louis, MO, USA). PCE (analytical grade > 98.5% purity) was purchased from Thermo Fisher Scientific (Waltham, MA, USA). CF (99.5% purity) was provided by Labscan Limited (Dublin, Ireland). The physical properties of TCE, PCE and CF are reported in Table 2 and the chemical structures in Fig. 1(b).

All experiments were performed in ultra-pure water with resistivity > 1 MΩ cm, at room temperature and all the compounds were used as received.

All spectrophotometric measurements were carried out by using a UV–VIS spectrophotometer (Agilent 8453, Agilent Technologies, Santa Clara (CA), USA).

2.2. Monitoring of hydrodynamic instabilities

To study the interfacial dynamics between DNAPLs and surfactant aqueous solutions, a quartz cuvette, having 1 mm thickness (1 × 10 × 50 mm), was used as a Hele-Shaw cell. In a typical experiment, two equal volumes of solutions with different densities were layered in the cell, as sketched in Fig. 2. The bottom one consists of the denser organic phase and the top one contains pure water or surfactant aqueous solutions. All experiments were carried out at room temperature (∼ 25 °C).

Table 1

Properties of the surfactants tested (MW = molecular weight; CMC = critical micelle concentration; D_B^T = diffusivity of the surfactant in the top aqueous phase; D_B^B = diffusivity of the surfactant in the bottom organic phase; $\partial_B \rho^T$ = density expansion coefficient of the surfactant in the aqueous phase; $\partial_B \rho^B$ = density expansion coefficient of the surfactant in the organic phase). MW and CMC were taken from: Rossi et al. (2008) C14-DMAO, Apte (2016) SDS, CTAB, AOT, Garza-Arévalo et al. (2019) Syn 91/5, Syn 91/10; D_B^T, D_B^B, $\partial_B \rho^T$, $\partial_B \rho^B$ were measured in this work.

	MW (g mol⁻¹)	CMC (M)	D_B^T (cm² s⁻¹)	D_B^B (cm² s⁻¹)	$\partial_B \rho^T$ (g cm⁻³ M⁻¹)	$\partial_B \rho^B$ (g cm⁻³ M⁻¹)
C14-DMAO	257.50	1.60×10^{-4}				
SDS	288.38	8.25×10^{-3}				
CTAB	365.45	9.2×10^{-4}				
Syn 91/5	378.54	8.24×10^{-4}				
AOT	444.56	6.4×10^{-4}				
Syn 91/10	598.80	6.10×10^{-4}	1.03×10^{-6}	1.30×10^{-5}	0.0365	−0.15

Table 2

Physical properties of the chlorinated organic compounds. D_A^T and $\partial_B \rho^T$ were measured in this work.

	MW (g mol⁻¹)	Density (g cm⁻³)	Water solubility (g L⁻¹)	D_A^T (cm² s⁻¹)	$\partial_B \rho^T$ (g cm⁻³ M⁻¹)
CF	119.38	1.49	8.09		
TCE	131.4	1.46	1.28	8.60×10^{-6}	0.0365
PCE	165.83	1.62	0.15		

Table 3

Maximal solubility of TCE in Syn 91/10 solutions, C_s^{TCE}, at ~25 °C.

Syn 91/10 (M)	C_s^{TCE} (M)
1×10^{-4}	9.74×10^{-3}
1×10^{-3}	0.011
0.01	0.04
0.05	0.15
0.08	0.26
0.10	0.33
0.15	0.45
0.20	0.64

Fig. 1. Chemical structure of (a) the surfactants and (b) organic solvents tested.

M-phase was prepared by layering 1 mL of [Syn 91/10] = 0.08 M on top of 1 mL of pure TCE followed by vigorous stirring for 1 h, finally the supernatant (M-phase) was transferred into a vial and used for analysis.

2.3. Solubility

The maximal solubility of PCE (C_s^{PCE}) in Syn 91/10 solutions was determined through the progressive addition of known amounts of PCE to water solutions at a given concentration of surfactant, followed by vigorous shaking, until a macroscopic phase-demixing took place (cloudy solutions). The last volumetric addition before the demixing process was used to calculate C_s^{PCE}. More details can be found in Intiso et al. (2018), Garza-Arévalo et al. (2019), where the same technique was employed to measure the maximum solubility of TCE (C_s^{TCE}) in Syn 91/5 and Syn 91/10 aqueous solutions, respectively (C_s^{TCE} for Syn 91/10 systems is reported in Table 3).

By applying the same procedure, the maximum solubility of pure Syn 91/10 ($C_s^{Syn91/10}$) and Syn 91/5 ($C_s^{Syn91/5}$) in the three chlorinated compounds was also assessed (see Table S7 in the SI).

2.4. Density

A thorough characterisation of the TCE/Syn 91/10 system density (ρ) was conducted for all the concentrations explored in the Hele-Shaw experiments. The measurements were carried out at 25 °C by using a high precision ($\pm 5 \times 10^{-6}$ g cm⁻³) Anton-Paar© DMA 5000 density meter. Solutions were prepared just before analysis to avoid TCE evaporation. The density of water and TCE solutions of Syn 91/10 were analysed in the concentration range 0.01–0.20 M, whilst the density of the ternary system (water/TCE/Syn 91/10) was determined at every C_s^{TCE} for each concentration of Syn 91/10 (see Table 3 and SI).

In diluted solutions, the density shows a linear relationship with the concentration of a varied species, [I], and the slope of this linear trend, $\partial_I \rho$, identifies the contribution of that species to the solution density. The solutal expansion coefficients $\partial_I \rho$ allow us to reconstruct the global density of a multicomponent system through the state
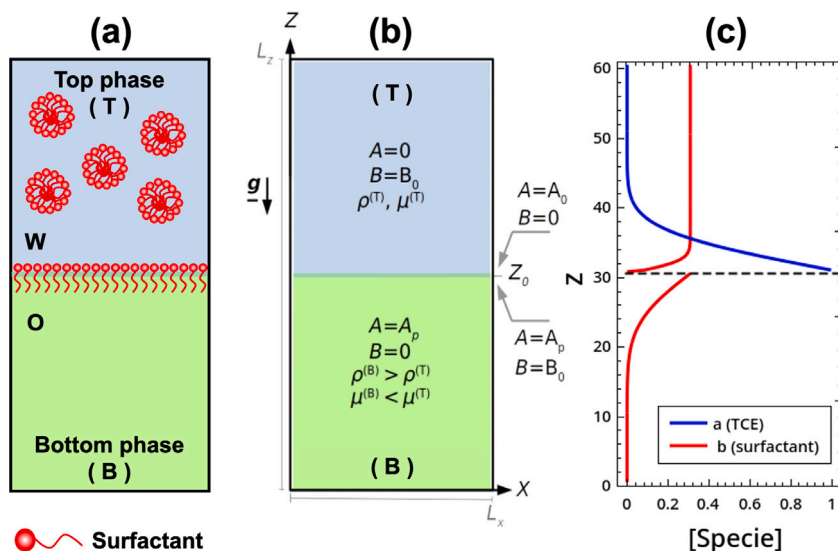
The spatiotemporal dynamics around the interface between the two layers were observed by using the schlieren technique (Joannes et al., 2003) which makes visible changes of the refractive index and gradients of density in otherwise colourless liquids. Our homemade setup (see the scheme illustrated in the supplementary movie) did not allow for quantitative measurements of the concentrations; however, the contrast between areas having different compositions was found qualitatively proportional to the difference of density, with darker areas corresponding to denser regions (see section 9 and Figure S9 in the SI). Images of the interface instabilities have been acquired through a CMOS camera (Imaging Source GmbH, Bremen, Germany) at 1–30 fps. Collected images were analysed by using the ImageJ software (Schneider et al., 2012).

To understand the role of the intermediate phase (M-phase), which forms across the layer interface by diffusive mixing of the aqueous and organic components before the onset of the instabilities, we performed some experiments by stratifying water solutions directly on top of the M-phase, poured in the Hele-Shaw cell in the place of the pure DNAPL.

Fig. 2. (a) Sketch of the initial configuration in the Hele-Shaw experiments. **W** is the top aqueous surfactant solution, **O** is the bottom organic (DNAPL) phase with $\rho_O > \rho_W$. (b) Basic features of the model for simulating the dissolution of a DNAPL (TCE, A) in an aqueous layer containing a surfactant (Syn 91/10, B). The aqueous solution of B with concentration B_0, initial density ρ^T and dynamic viscosity μ^T, is layered on top of the pure A (with concentration A_p, density $\rho^B > \rho^T$ and dynamic viscosity $\mu^B = \frac{1}{2}\mu^T$) which dissolves with constant concentration A_0 into the top phase. The surfactant B diffuses faster in the organic bottom phase than in the top aqueous phase ($D_B^T \sim 0.08 D_B^B$) and is slower than aqueous TCE in the top layer ($D_B^T \sim 0.12 D_A^T$). (c) Representative profiles of the dimensionless concentration of the chemical species A and B along the gravitational.

equation (Almarcha et al., 2011; Lemaigre et al., 2013)

$$\rho = \rho_0 \left(1 + \frac{1}{\rho_0} \sum_I I\, \partial_I \rho \right) \forall I\text{-th solute}, \tag{1}$$

ρ_0 being the solvent density. The density profiles along the gravitational axis can be used to interpret possible sources of buoyancy-driven convection (see Section 4) and, thus, $\partial_I \rho$ are key parameters for the system modelling. $\partial_I \rho$ for the main species used in the Hele-Shaw experiments are summarised in Tables 1 and 2.

2.5. Taylor dispersion analysis

Mutual diffusion coefficients D (cm^2 s^{-1}) of Syn 91/10 in pure TCE and water were measured by using the Taylor dispersion technique (Taylor, 1953; Alizadeh et al., 1980). A HPLC apparatus equipped with a refractive index detector (Infinity 1260 series, Agilent Technologies, Santa Clara (CA), USA) was adapted for the Taylor dispersion experiments (Vanag et al., 2008; Rossi et al., 2010, 2011). A 15 m silica glass capillary (inner radius $R_0 = 0.016 \pm 0.002$ cm), coiled in a 30 cm diameter helix, was used as the dispersion column. The capillary was placed in a thermostatted water-bath (Julabo ME-16G, Julabo GmbH, Seelbach, Germany), between the manual injector (Rheodyne 7125, IDEX, Lake Forest (IL), USA) and the thermostatted refractive index detector (Infinity 1260 series, Agilent Technologies, Santa Clara (CA), USA). Samples were injected by using a 20 μL sample loop every 25 min to avoid the overlapping of the peaks, being the retention time of the dispersion process $\sim$ 15 min, at constant flow = 0.1 mL min^{-1}. To determine the diffusivity of Syn 91/10 in water, D_B^T, aqueous surfactant solutions with a [Syn 91/10]= 0.08 M and 0.07 M were injected in an eluent with [Syn 91/10] = 0.05 M. To measure the diffusivity of Syn 91/10 in TCE, D_B^B, solutions of the surfactant at different concentrations (1×10^{-3} M<[Syn 91/10]<0.1 M) were prepared in pure TCE. The eluent was pure TCE. The distribution of concentration was monitored by a Refractive Index Detector (RID, Agilent G1362 A) and data were stored in a PC for analysis. For 2-component systems, the mutual coefficient D can be determined by fitting RID experimental signals with the following equation (Callendar and Leaist, 2006; Valletti et al., 2022):

$$S_{(t)} = S_0 + S_1 t + S_{max}\sqrt{\frac{t_r}{t}} exp\left[\frac{-12D(t-t_r)^2}{R_0^2 t}\right] \tag{2}$$

where $S_{(t)}$ (R.I.U. units) is the experimental refractive index signal, S_0 (R.I.U. units) and S_1 (R.I.U. units) are the intercept and the slope of the linear baseline, respectively, S_{max} (R.I.U. units) is the peak height, t_r (s) is the retention time, R_0 (cm) is the inner capillary radius and t (s) is the time. Multiple experimental peaks were simultaneously fitted using Levenberg–Marquardt algorithm (Marquardt, 1963; Levenberg, 1944) to Eq. (2). The measurements of the surfactant diffusivity in water and in the organic phase (TCE) are further described and reported in the SI.

2.6. Interfacial tension

The interfacial tension analysis was carried out using the pendant drop method (OCA 15 PLUS by DataPhysics). The aqueous solutions of the surfactants were analysed in a concentration range of 0.0001–0.0250 M for Synperonic™ 91/10. The measurements were carried out by producing a drop of chloroform (as an example of DNAPL) in a Syn 91/10 solution and getting measurements until equilibrium at 25 °C using a 0.51 mm diameter capillary.

2.7. Model

We consider a two-dimensional two-phase system of length L_X and height L_Z in a (X, Z) reference frame, where the Z axis is oriented vertically against the gravitational acceleration $\mathbf{g} = (0, -g)$. The system is supposed to be in isothermal conditions. The denser organic layer with the pure DNAPL (TCE, A) is in the bottom (B) while the less dense aqueous phase containing the surfactant (Syn 91/10, B) is stratified on top (T) as sketched in Fig. 2(b) and specified by the initial spatial distribution of the species concentrations

$$(A, B) = (A_p, 0) \text{ for } Z < Z_0 = L_Z/2 \ \forall X$$
$$(A, B) = (0, B_0) \text{ for } Z > Z_0 \ \forall X,$$
$$(A, B) = (A_0, 0) \text{ for } Z = Z_0 \ \forall X$$
$$(A, B) = (A_p, B_0) \text{ for } Z = Z_0^- \ \forall X$$

$$\text{i.e. just below the interface}, \tag{3}$$

A_p is the concentration of the pure TCE and A_0 represents the saturation concentration of TCE in an aqueous layer containing the surfactant with concentration B_0. From Table 3, the empirical relation $A_0 \sim B_0/3$ can

be inferred. In our model, we keep A_0 constant at the interface between the two phases to mimic the constant amount of TCE coming from the solubilisation of the pure bottom phase which, under the hypothesis of local equilibrium, rapidly attains the saturation value (Loodts et al., 2014; Budroni et al., 2014, 2017).

Similarly, as the surfactant is highly soluble in TCE, we assume that the organic phase acts as a sink for the surfactant whose concentrations go locally to zero at $Z = Z_0$ and to B_0 in the organic layer, just below the interface at $Z = Z_0^-$ (see Fig. 2(c)). As the upward drifting of the interface is negligible within the hydrodynamic time scale and the surface tension along the contact line between the two layers is assumed to be high enough to render negligible any deformation of the interface and the layer frames are kept fixed.

The dynamics around the interface was investigated numerically by solving the sets of dimensionless diffusion–convection (DC) equations which describe the two coupled phases (Bratsun and De Wit, 2004; Lemaigre et al., 2013; Budroni et al., 2014, 2021):

(Top layer)

$$\partial_t a^T + (\partial_z \psi^T) \partial_x a^T - (\partial_x \psi^T) \partial_z a^T = \nabla^2 a^T, \tag{4}$$

$$\partial_t b^T + (\partial_z \psi^T) \partial_x b^T - (\partial_x \psi^T) \partial_z b^T = \delta_b^T \nabla^2 b^T, \tag{5}$$

$$\partial_t \omega^T + (\partial_z \psi^T) \partial_x \omega^T - (\partial_x \psi^T) \partial_z \omega^T = \tag{6}$$

$$S_c^T \left(\nabla^2 \omega^T - \sum_{i=a,b} R_i^T \partial_x i^T \right)$$

$$\nabla^2 \psi^T = -\omega^T, \tag{7}$$

(Bottom layer)

$$\partial_t b^B + (\partial_z \psi^B) \partial_x b^B - (\partial_x \psi^B) \partial_z b^B = \delta_b^B \nabla^2 b^B, \tag{8}$$

$$\partial_t \omega^B + (\partial_z \psi^B) \partial_x \omega^B - (\partial_x \psi^B) \partial_z \omega^B = \tag{9}$$

$$S_c^B \left(\nabla^2 \omega^B - R_b^B \partial_x b^B \right)$$

$$\nabla^2 \psi^B = -\omega^B. \tag{10}$$

Here $i = a, b$ represent the dimensionless concentrations of the chemical species A and B, scaled by the saturation concentration of TCE in the surfactant aqueous solution, A_0. The evolution of the chemical fields described by Eq. (4)–(5) and (8) are coupled to Fickian diffusion and to incompressible Navier–Stokes Eqs. (6)–(7) and (9)–(10) written in the *stream function–vorticity* ($\psi - \omega$) form according to the Boussinesq approximation. The vorticity and the stream function describe the hydrodynamics of the system being related to the velocity field $\mathbf{v} = (u, v)$ *via* $\omega = \nabla \times \mathbf{v}$ and $u = \partial_z \psi$ and $v = -\partial_x \psi$, respectively.

No-flux boundary conditions and no-slip conditions are used for the chemical concentrations and the stream function at the rigid boundaries of the reactor, respectively. At the interface between the two phases (i.e. $z = z_0$) we consider

$$a^T = A/A_0 = 1, \tag{11}$$

$$b^T = 0, \tag{12}$$

$$\psi^T = \psi^B = 0, \tag{13}$$

$b^B(z_0^-) = b^T(z_0^+)$ and the Marangoni boundary condition $\eta \omega^T = \omega^B = \sum_{i=a,b} M_i \partial_x i_s^B$ (where i_s are the concentrations of the chemical species a and b at $z = z_0^-$, and $\eta = \mu^T/\mu^B$, with μ^T and μ^B representing the dynamic viscosity of the aqueous and organic phases, respectively).

This condition couples the hydrodynamics between the two phases and, along with the gravitational force terms $\sum_{i=a,b} R_i^T \partial_x i^T$ and $R_b^T \partial_x b^B$, relates the evolution of the chemical fields to the vorticity and the stream function.

Key parameters to control the onset of convective instabilities and related impact in the dissolution dynamics are the solutal Rayleigh numbers of the I–th species, defined as

$$R_i^T = \frac{\partial_I \rho^T A_0 g L_0^3}{D_A \mu^T}, i = a, b, \tag{14}$$

in the top layer, and

$$R_i^B = \frac{\partial_I \rho^B A_0 g L_0^3}{D_A \mu^B}, i = a, b, \tag{15}$$

in the bottom phase.

These parameters weight the specific contribution of each species concentration to the local dimensionless densities, $\tilde{\rho}^T = \sum_{i=a,b} R_i^T i$ and $\tilde{\rho}^B = R_b^B b$. The Rayleigh numbers control the onset and entity of buoyancy-driven convection in response to chemical concentration gradients. Since in the bottom phase we have TCE as a pure liquid, the Rayleigh number for this species can be only defined in the top phase and the DC equation for a is only considered for that layer. L_0 is the characteristic spatial scale of the system, here corresponding to the width of the Hele-Shaw cell used in the experiments ($L_0 = 1$ cm); the coefficients $\partial_I \rho^T$ and $\partial_I \rho^B$ measure the density change due to small variations in the concentration of the I–th species in the top and the bottom layer, respectively. D_A is the diffusion coefficient of TCE in the upper phase and can be used to define the time scale of the system, $t_0 = L_0^2/D_A$. $\delta_b^T = D_B^T/D_A$ and $\delta_b^B = D_B^B/D_A$ are the dimensionless relative diffusivities of the surfactant in the top and bottom layers, respectively.

Another important parameter is the solutal Marangoni number

$$M_i = -\frac{A_0 L_0}{\mu^B D_A} \partial_I \gamma, \tag{16}$$

which quantifies the specific contribution of the I–th species to the dimensionless surface tension $\tilde{\gamma} = -\sum_{i=a,b} M_i i_s$ and controls the entity of transversal flows at the partially miscible interface due to the transfer of chemical species from one phase to the other. In our simulations we assume that the surfactant plays the main role in surface tension changes, i.e we considered $M_a = 0$ and $M_b > 0$, as b is supposed to decrease the surface tension.

We also run check simulations by applying no-slip boundary conditions to the vorticity and ψ-function at the interface in order to have a reference case where surface tension stresses are not at play and evaluate their actual weight in the global dynamics.

The coupled systems of DC Eqs. (4)–(7) and (8)–(10) are solved numerically by using the Alternating Direction Implicit Method (ADI) (Peaceman and Rachford, 1955) over the spatial domain of length $L_x = 30 L_0$ and height $L_z = 2 L_x$ (i.e. aspect ratio 2), by using a space meshing $h_x = h_z = 0.1$ and the integration time step $h_t = 1 \times 10^{-4}$.

The numerical algorithm is particularly stable for 2-dimensional problems and squared meshings. It consists of solving explicitly the derivatives along one spatial dimension (for instance along the x-axis) and implicitly in the second one (z). The direction along which the implicit and the explicit descriptions are employed is alternated during each successive iteration, which corresponds to one-half time step. At any given iteration, the unknowns of each single equation are the implicitly calculated variables, solved as a function of the explicitly calculated terms. To solve the hydrodynamic field, an iterative procedure checks the convergence of ω and ψ over the entire spatial domain, requiring the error between the stream function at the $(n - 1)$-th and (n)-th iterations to be lower than 1×10^{-5}.

3. Results

To mimic a stratification of an aqueous solution over a denser organic solvent in a porous medium, we employed a vertical Hele-Shaw cell arranged as in Fig. 2a. In a series of experiments, the DNAPL was poured at the bottom of the cell and a less dense water solution, containing an increasing amount of surfactant, was gently poured on top of it. In general, the presence of the surfactant at a concentration larger than the CMC increases the solubility of the DNAPL in the upper aqueous layer (Table 3 and Table S6 in the SI) and, at the same time, decreases the interfacial tension (Table S8 and Figure S11 in the SI). For the sake of simplicity, in this section, we will focus on the system

TCE/Syn 91/10, but similar results, though for a slightly different interval of concentrations, were obtained for the system TCE/Syn 91/5.

Given the low reciprocal solubility of the two liquids and the surface tension between the two liquids, this density stratification is expected to be statically stable in the gravity field. In fact, up to a threshold concentration of [SYN 91/10] = 1×10^{-2} M the interface remained unperturbed and the mass transfer of the TCE to the aqueous layer took place by diffusion only. Interestingly, in experiments where the concentration of SYN 91/10 was higher than 1×10^{-2} M, ascending plumes of TCE developed despite the fact that the initial density of the top layer was lower than that of the bottom one.

These scenarios are illustrated in Fig. 3 which shows the experimental schlieren images of systems where Syn 91/10 aqueous solutions at different concentrations are layered on top of pure TCE. In the case of [Syn 91/10] = 1×10^{-3} M (bottom panels in Fig. 3), the interface remained stable for the entire course of the experiment and the appearance of some blurred dark areas, above and below the interface, could be noticed. The schlieren technique allows to enhance the contrast of transparent fluids according to their refractive index (and hence density), therefore the darkening of the liquids around the interface tracks the displacement of the chemical species across the contact line between the two phases with a consequent change of the local density. The timescale characterising the thickening of the interface (an average displacement of ~ 2 mm in 3000 s can be measured from the bottom panels of Fig. 3) allows to ascribe to Fickian diffusion the mixing in these experimental conditions ($t = d^2/2D$, where d is the mean square displacement and D is the diffusion coefficient, which for small molecules in liquids is generally of the order of 10^{-6}–10^{-5} cm^2/s).

When the concentration of Syn 91/10 in the water phase was larger than $\sim 1 \times 10^{-2}$ M, hydrodynamic instabilities appeared just below and above the liquid–liquid interface after a few minutes from the beginning of the experiment. The top and the central panels of Fig. 3 show the formation of TCE plumes developing in the less dense water phase and displacing at a constant speed. As typically happens in fingering instabilities (Lemaigre et al., 2013; Budroni et al., 2017), plumes grew linearly in time and the related displacement speed (V_m) could be calculated from experimental Space-Time (ST) plots according to the procedure reported in Section 10 of the SI. The averaged value of V_m for each system has been reported in Fig. 4 (a) (and in Table S1 of the SI) as a function of [Syn 91/10]. Interestingly, V_m also showed a linear dependence on the concentration of the surfactant in the water phase ($V_m = m$[Syn 91/10] $+ q$, $m = 0.15 \pm 0.01$ (mm M^{-1} s^{-1}), $q = 9.47 \pm 0.9 \times 10^{-3}$ (mm s^{-1}) and R^2= 0.97608). By comparing the speed at which fingers grew from the organic into the aqueous phase, the mixing rate resulted from 10 to 40 times – depending on [Syn 91/10] – faster than that due to the Fickian diffusion (average displacement of TCE molecules $\sim 8 \times 10^{-4}$ mm/s).

In general plumes and fingering instabilities around an initially stable stratified liquid–liquid interface are due to an inversion of the local density (Almarcha et al., 2011; Trevelian et al., 2011; Budroni et al., 2014) and we will discuss the mechanism in more details in the next section. It has to be noted that, in the TCE/Syn 91/10 system, the development of the plumes was accompanied by periodic pulsations which took place just below the interface and originated from a Marangoni-type instability sustained by surfactant-induced gradients in the surface tension. Fig. 4b (and the supplementary movie) shows the development of a pulsation in a TCE/Syn 91/10 system where [Syn 91/10] = 0.08 M. The pulse nucleated from the sides of the Hele-Shaw cell and developed horizontally towards the centre. Similar dynamics have been observed at the interface of partially miscible stratifications of alkyl-formates layered on top of aqueous solutions (Budroni et al., 2014, 2017). The dark colour was certainly due to the surfactant (and possibly some water) which was partitioned in the DNAPL phase. Marangoni pulses showed a quite regular dynamics with a characteristic period of ~ 500 s, as shown in the time-series reported in Fig. 4c. The synergy between the plumes and the Marangoni pulses transiently favoured the mixing

of the two phases resulting in an enhanced dissolution of the DNAPL in the aqueous layer.

In all the systems where instabilities occurred, the formation of a new surfactant-rich-middle-phase (M-phase) at the contact zone between the water and the DNAPL was observed just before the appearance of the instabilities (dark interfacial area at $t = 1000$ s in the top and middle panels of Fig. 3). The M-phase appeared milky and with a high turbidity and it was characterised as a thermodynamically unstable macroemulsion (Winsor type III system) (Kang et al., 2019; Lagzi, 2015). The M-phase and its role in the onset of the instability have been extensively discussed in the section S7 of the SI.

The convective stability of aqueous surfactant solutions stratified on top of a DNAPL was further investigated by changing the organic liquid. When chloroform was employed, hydrodynamic patterns similar to the TCE case were obtained. By contrast, statically stable stratifications were found for PCE at all the concentrations of surfactant monitored (see Figure S4 in the SI).

Finally, the presence of plumes and fingers was further explored for other classes of surfactants. We tested the anionic SDS and AOT, the cationic CTAB and the zwitterionic C14DMAO, all of them (or very similar molecules) were reported to enhance the solubility of DNAPLs in water solutions (Harendra and Vipulanandan, 2011; Acosta and Quraishi, 2014; Mao et al., 2015). The experimental setup was kept fixed and we used TCE as the organic phase. Instabilities with a low intensity were detected only when the water phase contained [AOT] > 0.03 M (see Figure S5 in the SI), for the rest of the surfactants no clear instabilities could be observed. Interestingly, the formation of an M-phase was found also in the TCE/AOT system, though it was found denser and less persistent with respect to the M-phase generated by the exthoxylated surfactants.

4. Discussion

4.1. Interpretation of the hydrodynamic instability

The onset of the fingering instability stems from the inversion of the local density just above the interface between the two layers. According to the chemico-physical parameters measured for the species at play (see details in the SI: section S2 for density, section S3 for diffusivity and section S4 for solubility) we envisaged the following mechanism (see also the supplementary movie).

First, plumes were always located in the top layer and must be originated from a local density depletion just above the contact line between the two phases. In principle, this could be provided by the downward migration of the surfactant into the bottom organic layer where it is highly soluble either in the form of micellar aggregates or in the form of monomers. The chemical structure of ethoxylated alcohols is, in fact, known to favour the partition of the surfactant in the DNAPL phase (Zhu and Free, 2015) as a function of the number of ethylene oxide (EO) units (Zimmerman et al., 1999). Both Syn 91/10 and Syn 91/5 were found to be largely soluble in TCE at 25 °C and miscible in all proportions with it. The affinity of Syn 91/10 for TCE was also confirmed by measuring the diffusivity of the surfactant in water and in the organic phase: D_B^T (in the aqueous phase) was 1.03×10^{-6} cm^2 s^{-1} and D_B^B (in TCE) was 1.30×10^{-5} cm^2 s^{-1}, as determined by the Taylor dispersion technique (see Section 2.5 and section S3 in the SI).

The organic phase acted thus as a sink for the surfactant (see the red profile in Fig. 2c, but the related density depletion was largely compensated by the counter dissolution of TCE. In fact, though $\frac{\partial \rho^T}{\partial [\text{TCE}]} \sim \frac{\partial \rho^T}{\partial [\text{Syn 91/10}]}$ (see Tables 1, 2 and section 2 of the SI), TCE provided a larger contribution to the density according to Eq. (1) because its aqueous concentration was higher than that of the surfactant (about 3 times), and this determined a stable downward increasing density profile of the type shown in the left panel of Fig. 5.

However, the local drop of the surfactant concentration at the interface created a concentration gradient which broke *de facto* the initial
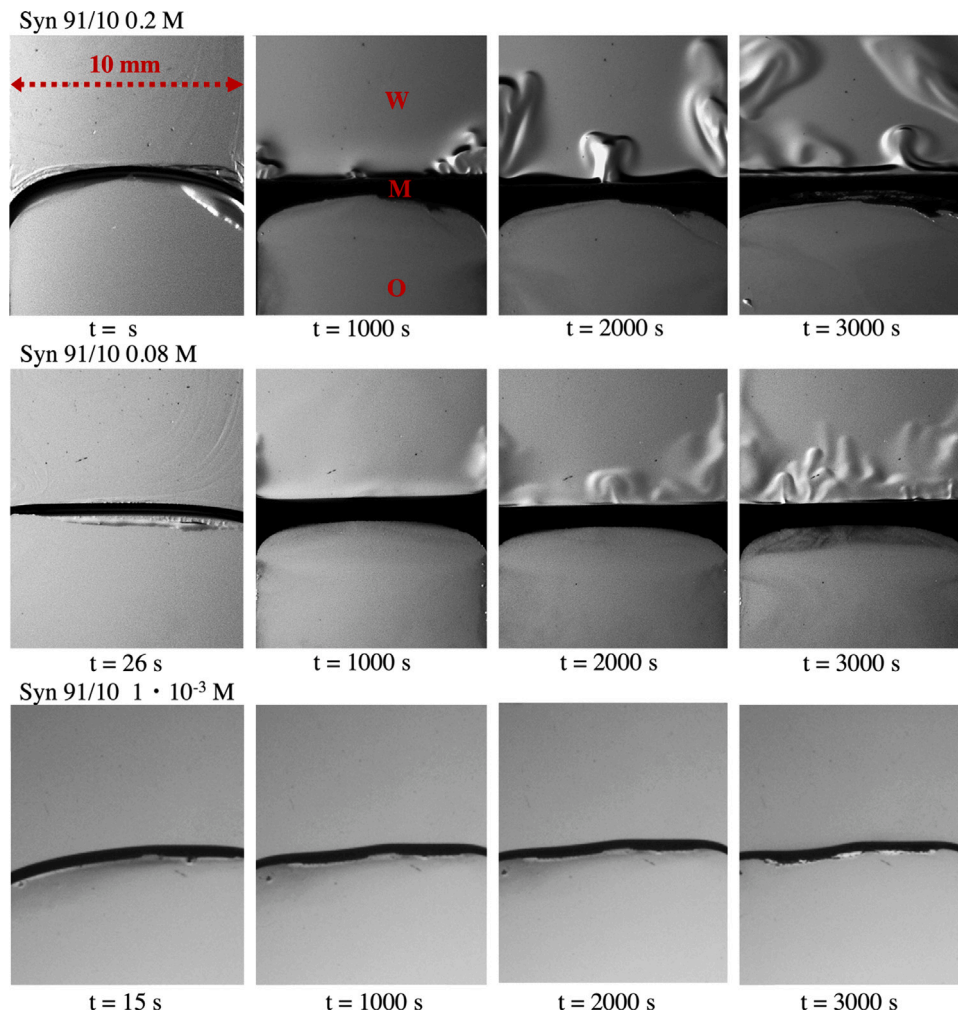
Fig. 3. Snapshots describing the development of the fingering instability in representative systems with different [Syn 91/10]. O, W, and M stand for the organic phase, water solution and the middle-surfactant-rich-phase, respectively. The M-phase starts to form in the aqueous solution, above the interface. Instabilities generally start after ∼ 15 min from the phases contact at [Syn 91/10] = 0.20 M and [Syn 91/10] = 0.08 M. The M-phase formation and the instabilities are absent at [Syn 91/10] = 1×10^{-3} M. Frame size is 10×12 mm^2.
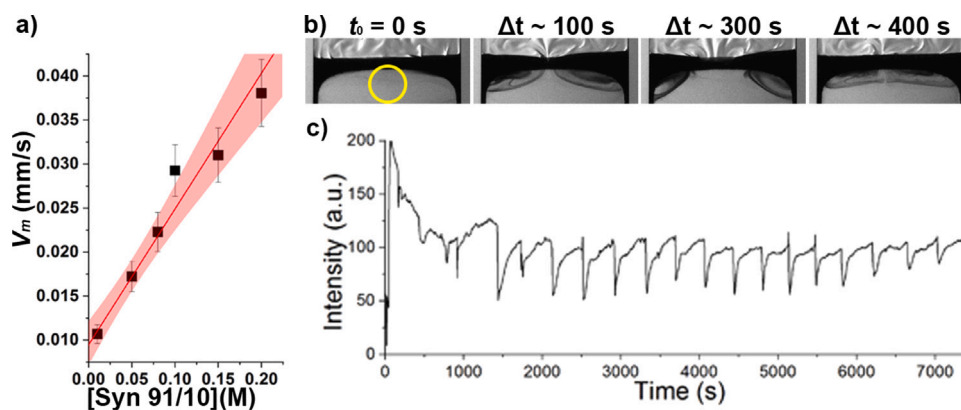
Fig. 4. (a) Speed of plumes growth (V_m) at different [Syn 91/10]. The red line represents the best linear fitting of the experimental data (R^2= 0.97608); (b) development of a Marangoni pulse in the organic phase, just underneath the interface in a system containing [Syn 91/10] = 0.08 M in the water phase; (c) time-series reporting the periodic Marangoni pulsations recorded by measuring the average pixel intensity in the area comprised by the yellow circle in panel (b). (For interpretation of the references to colour in this figure legend, the reader is referred to the web version of this article.)

convective stability by starting a differential diffusive interplay in the aqueous layer between the fast upwardly-diffusing TCE ($D_A = 8.16 \times 10^{-6}$ cm^2 s^{-1} (Rossi et al., 2015)) and the slow downward-diffusing surfactant ($D_B^T = 1.03 \times 10^{-6}$ cm^2 s^{-1}). In time, this developed a non-monotonic density profile with a local density minimum as shown

in the right panel of Fig. 5, sustained by a delayed double-diffusive mechanism (Trevelian et al., 2011).

Furthermore, the concurrent transfer of TCE and surfactant between the two phases modified the interfacial tension between the two liquids and caused transversal Marangoni stresses (Sternling and
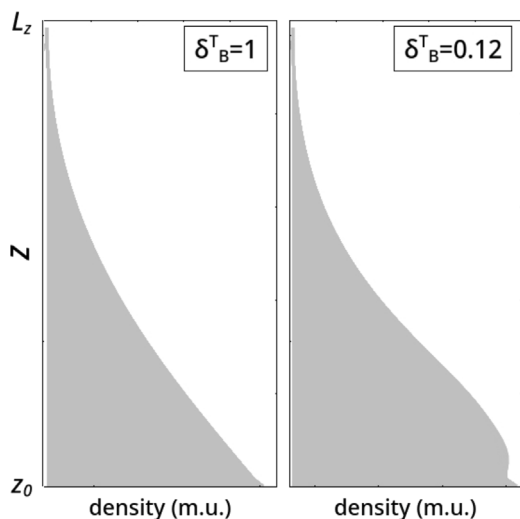
Fig. 5. Comparison between the downward-increasing density profile of the top aqueous layer ($z \in [z_0, L_z]$) when $D_A^T \sim D_B^T$ ($\delta_b^T = 1$, left) and the non-monotonic density profile developing in the presence of the double-diffusion scenario ($D_A^T > D_B^T$, $\delta_b^T = 0.12$, right) characterising our experimental system. Density profiles, expressed in dimensionless model units, are obtained by integrating Eqs. (4)–(10), taking horizontally averaged (along x) profiles of the chemical concentrations and plugging these into the density Eq. (1). These results are for $t = 40$ time model units.

Scriven, 1959; Bratsun and De Wit, 2004), as manifested by the periodic pulsations at the interface. The dissolution of the Syn 91/10 did not create any buoyancy-driven instabilities in the lower organic layer because it was characterised by a negative contribution to the density ($\frac{\partial \rho^B}{[\text{Syn 91/10}]} \sim -0.15$ g cm^{-3} M^{-1}).

Our interpretation based on the solubility of the surfactant and on the DNAPL-surfactant differential diffusion, can explain the different behaviours observed when other surfactants (SDS, AOT, CTAB and C14DMAO) replaced the ethoxylated alcohols in the aqueous layer and when other DNAPLs (CF and PCE) replaced the TCE.

In the case of alternative surfactants, instabilities were observed for AOT only; this was due to the fact that AOT has a similar phase-behaviour of Syn 91/10 and Syn 91/5, i.e. high solubility in the organic phase and it is able to form microemulsion without the need of a co-surfactant (Broze and Zoller, 1999; Mao et al., 2015). Moreover, the other surfactants have a lower molecular weight than Syn 91/10 and Syn 91/5 (see Table 1), which is reflected into a higher diffusivity in water that suppressed the differential diffusion mechanism.

Concerning the experiments with alternative DNAPLs, instabilities were found only for CF which, in contrast to PCE, has physico-chemical characteristics similar to those of TCE (density and miscibility with surfactants). PCE is, in fact, much denser and by far less miscible both in water and in surfactant solutions than TCE (see Table 2 and Table S6 in the SI for the saturation concentration of PCE, C_s^{PCE}).

We finally note that a fingering instability in analogous systems could also be activated without differential diffusion if the contribution to the density of the DNAPL in the aqueous phase, ($\frac{\partial \rho^T}{[\text{DNAPL}]}$), would be much lower than that of the surfactant at hands. Then a density minimum would simply develop due to the surfactant solubilisation into the underlying organic layer.

4.2. Nonlinear simulations

To support the mechanism proposed for the onset of hydrodynamic instabilities, we run numerical simulations by feeding the theoretical model described in Section 2.7 with the experimental chemico-physical parameters measured in the experiments.

We set $S_c^T = 10000$, which is compatible with the water kinematic viscosity ($\nu^T = \mu^T/\rho_0 = 0.0089$ cm^2 s^{-1}) and with the aqueous diffusivity of TCE, while S_c^B was fixed to 5000 as $\nu^B \simeq 0.5\nu^T$.

As mentioned above, the coefficients $\partial_I \rho$ of TCE and Syn 91/10 in the aqueous phase, extrapolated as described in Section 2.4, presented analogous values ($\frac{\partial \rho^T}{\partial [\text{TCE}]} \simeq \frac{\partial \rho^T}{\partial [\text{Syn 91/10}]} = 0.0365$ g cm^{-3} M^{-1}) such that we could assume $R_a^T = R_b^T$. Realistic Rayleigh numbers (given $A_0 = 0.3$ M, $L_0 = 1$ cm and $D_A = 8.16 \times 10^{-6}$ cm^2 s^{-1}, $g = 9.8$ cm s^{-2}) have an order of magnitude 10^6, which is consistent with the appearance of short-wavelength convective fingering in the narrow spatial domain used in the experiments, 1 cm × 2 cm, corresponding to 1×2 model space units (L_0). However, to avoid numerical divergence, simulations with such high values would require an extremely refined spatio-temporal solving grid and a sensitive reduction of the error tolerance for the stream function computation (see Section 2.7), which is critically demanding from the computational viewpoint. We thus considered a spatial domain of 30×60 L_0, which, without loss of generality, allowed reproducing convective patterns similar to those of the experiments and to give a qualitatively consistent description of these phenomena even using lower values of the Rayleigh numbers. After a preliminary exploration, we fixed $R_a^T = R_b^T = 100$ and, since in TCE $\frac{\partial \rho^B}{\partial [\text{Syn 91/10}]} \sim -0.15$ g cm^{-3} M^{-1} and $\mu^B = 0.5\mu^T$, we set $R_b^B = -1000 = -10R_b^T$.

The measured values for D_A, D_B^T and D_B^B (see Tables 1 and 2 and section 3 in the SI) were used to define the dimensionless relative diffusivities of the surfactant in the top layer, $\delta_b^T = 0.12$, and in the bottom layer, $\delta_b^B = 1.51$. We finally varied $M_b \in (0, 50000]$ to check the relative importance of surface effects in the convective dissolution of TCE.

In Fig. 6 (see also the supplementary movie), we illustrate a typical spatio-temporal evolution of the dissolution-driven convective instability obtained with the parameter set $\{R_a^T = R_b^T = 100, R_b^B = -10R_b^T = -1000, M_b = 50000\}$. The snapshots show the vorticity in the top phase and just below the interface at different times. After an initial diffusive transient, plumes nucleated and grew upwardly above the interface. Similarly to the experiments, the plumes underwent some lateral merging, promoted by Marangoni flows below z_0. The transfer of surfactant between the two phases, in fact, generated surface-tension driven instabilities in the form of transversal pulses at the interface, which distorted the plumes in the top layer and could eventually homogenise them. Successively, plumes formed and rised again affected by surface tension-driven stresses. In particular, they formed at the lateral border of the spatial domain, where horizontal short pulses and drifting plumes were observed. These dynamics cannot be observed if we run simulations with $\delta_b^T > 0.35$, i.e. suppressing differential diffusion.

An overview of the global dynamics could be captured by using the ST plots (see section 10 of the SI) obtained by stacking as a function of the time the transversal profile of the vorticity just above and below the interface (white dashed lines in the first snapshot of the top panels of Fig. 6). These plots, shown in bottom panels of Fig. 6, represent the dynamics for 300 time units (thus dimension $L_x \times 300$ t_0) and show the main features of the convective instability: plumes started at $t^* \sim 63$ time units accompanied by Marangoni-driven horizontal pulses. The latter flows may disrupt the growth of the plumes and start pulsations towards the lateral borders of the spatial domain, as described by local zig-zag patterns along the borders. The dynamics below the interface was characterised by periodic pulsations, consistent with the experimental observations.

ST plots allow a direct comparison of the characteristic wavelength and onset time of the instability for different control parameters of the system, as reported in section 8 of the SI.

To make a direct comparison with the experiments, we characterised in Fig. 7 the speed of the fingering growth as a function of A_0 which is related to the surfactant concentration B_0 as $A_0 \sim B_0/3$. A_0
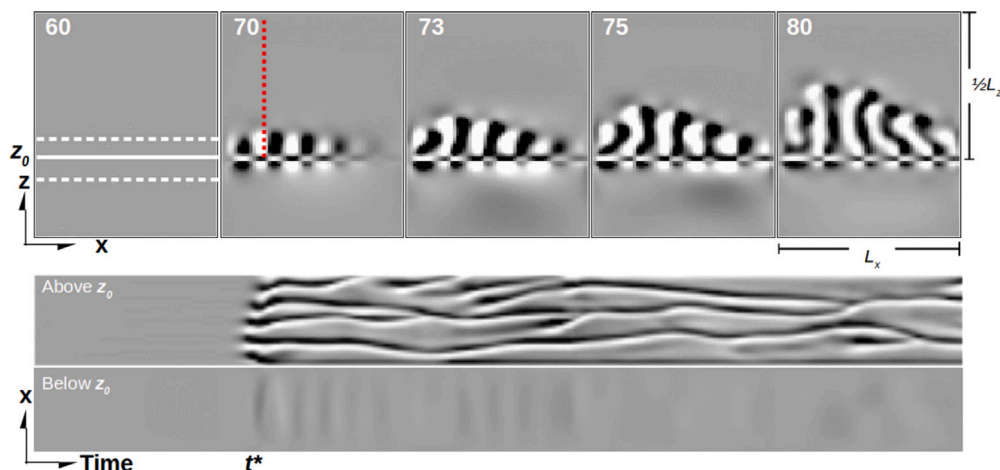
Fig. 6. (a) Snapshots describing the spatio-temporal evolution of the vorticity, $\omega(\mathbf{x}, t)$, during the convective dissolution obtained with the parameter set $\{R_a^T = R_b^T = 100, R_b^B = -10R_b^T = -1000, M_b = 50000\}$. Each snapshot frames the spatial domain $x \in [0, L_x]; z \in [\frac{L_z}{4}, L_z]$ and the vorticity ranges between -5 and 5. (b) Spacetime plots ($L_x \times 300\ t_0$) of the dynamics shown in (a) taken by staking as a function of the time the vorticity along the horizontal white lines shown in the first snapshot above and below z_0. t^* indicates the initial diffusive transient before the onset of convective plumes. The red dashed line in the second snapshot of the top panel locates the vertical section through which the fingering growth is followed and evaluated according to the procedure described in section 10 of the SI. (For interpretation of the references to colour in this figure legend, the reader is referred to the web version of this article.)

also controls both the Rayleigh and the Marangoni numbers (see definitions 14, 15, 16) and the impact of the initial surfactant concentration explored in the experiments could thus be reproduced numerically by changing proportionally R_i^T, R_b^B and M_b. The system specified by the parameter set $\{R_a^T = R_b^T = 100, R_b^B = -10R_b^T = -1000, M_b = 50000\}$ was associated to a relative reference value $A_0 = A_0^{ref}$ and compared with dissolution-driven convective dynamics obtained with decreasing fractions of these reference values. ST plots, built by following the development of the fastest plumes along the vertical axis (see the vertical dashed red line in the second snapshot of Fig. 6), showed that the plumes grew linearly in time, with a speed, V_m, that relates linearly with A_0 and, in turn, with the surfactant concentration B_0 (see Fig. 7a). This compares favourably with experimental analysis (cfr. Fig. 4a.)

To analyse the impact of the different contributions to convective flows in the dissolution of A, we also computed the mean flux J through $z = z_0^+$, averaged over the horizontal dimension x (Jotkar et al., 2019)

$$J = \frac{1}{L_x} \int_{x=0}^{L_x} \left(\frac{\partial a}{\partial z} \right)_{z=z_0^+} dx, \tag{17}$$

and we considered how this quantity varied as a function of the time for different values of A_0. In particular, in Fig. 7b, we report the temporal profile of $\Delta J(t)$, i.e. the difference between the flux obtained in systems with convection ($J(t)$) and the diffusive reference flux ($J_{\text{diff}}(t)$). In all cases, there was an initial spike due to the onset of convective instabilities followed by a decline to a rather constant flux (around 0.008 ± 0.002) over which all curves converged and fluctuated. A faster and stronger divergence from the purely diffusive dynamics was obtained for $A_0 = A_0^{ref}$, and progressively smooth-down when decreasing A_0.

To disentangle the role of the main contributions to the flow (i.e. buoyancy- vs Marangoni-driven flows), we characterised the instabilities developing with different values of $M_b \in (0, 500000]$ (with fixed $Ra_i^T = 100$, $Ra_b^B = -10Ra_i^T$, $i = a, b$) and in the absence of surface stresses at the contact line between the two phases. The results, reported in section 8 of the SI, show that, while the density-driven fingering always enhanced the dissolution process, Marangoni-driven flows, due to their orthogonal orientation with respect to the dissolution direction, may play either a positive, neutral or even unfavourable role with respect to the dissolution process. Indeed, Marangoni pulses favoured an initial enhancement of the flux, but this was followed by a drop due to the homogenising effect of these transverse flows which

suppressed the buoyancy-driven plumes. The successive formation of new convective plumes reinforced the dissolution flux again.

In general, the most unstable systems from a convective viewpoint which can be achieved by augmenting A_0 may not necessarily enhance the dissolution process as A_0 increases all the contributions to the flow unconditionally, including transversal flows. This information turns useful to orient the choice and the concentration of the surfactant to be employed. Similar conclusions were drawn in previous studies on convective dissolution in binary systems with partially miscible components (Lappa et al., 2005).

5. Conclusion

In this paper, we reported about hydrodynamic instabilities taking place at the interface of an initially stable stratification of a water solution on top of a denser pure DNAPL phase. In the case of pure water, given the reciprocal low solubility of the two liquids, the stratification was stable over time and the mixing between the two phases took place by molecular diffusion until the saturation concentrations were attained. This resemble the typical situation happening when a spill of a DNAPL from the surface penetrates into the soil until it stratifies below groundwaters to form a permanent source of pollution.

However, further investigations in a vertical Hele-shaw cell, revealed that the presence of suitable surfactants promoted an inversion of the local densities thus allowing for a faster mixing between the two phases; in particular, surfactants induced a massive transport of the DNAPL in the aqueous solution in the form of upward plumes and fingers.

The surfactant had three main roles, (i) it promoted the solubilisation of the DNAPL by forming micelles and microemulsion, (ii) it lowered the surface tension between the two phases to promote Marangoni effects and (iii) it favoured the inversion of the local density at the interface. The onset of the hydrodynamic instabilities was initiated by the fast diffusion and the high solubility of the surfactant in the organic phase which, combined to a double diffusion mechanism between the surfactant itself and the fast-diffusive TCE, decreased the density of the top aqueous layer in the proximity of the interface. At the same time, the changes of the surface tension induced periodic Marangoni pulsations in the DNAPL phase which interacted with the density driven advective motion. We thoroughly characterised the chemico-physical properties of the investigated systems (solubility, density, diffusivity, etc.) and we employed these parameters to feed
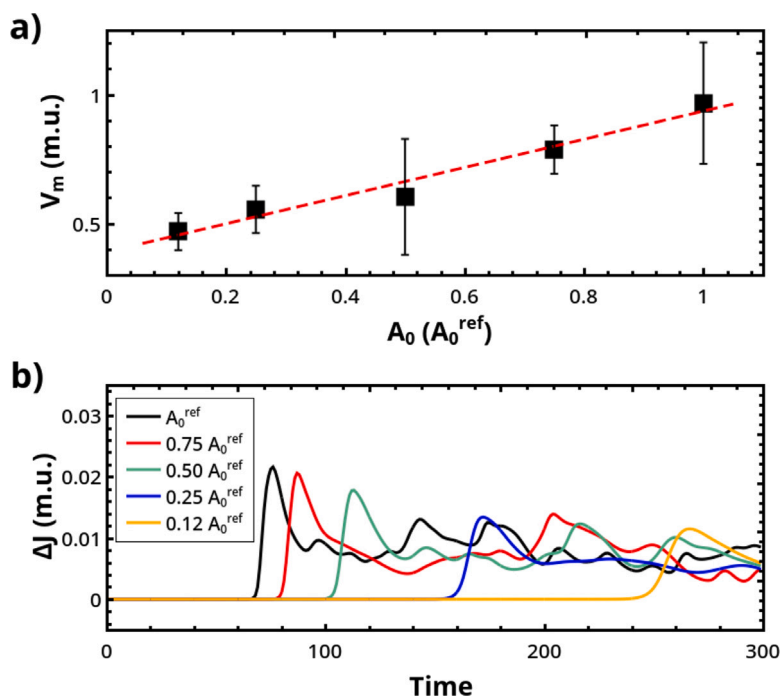
Fig. 7. Characterisation of the convective instability growth for different values of A_0, referred to the relative value A_0^{ref} corresponding to the parameter set $\{R_a^T = R_b^T = 100, R_b^B = -10R_b^T = -1000, M_b = 50000\}$. Panel (a) provides a quantitative analysis of the finger speed, V_m (expressed in dimensionless model units, m.u.), evaluated along the red dashed line shown in the second snapshot of Fig. 6 with the procedure described in section 10 of the SI. The red line represents the best linear fitting of the simulations data (R^2= 0.98824). Panel (b) compares the differential fluxes ΔJ of species A (expressed in dimensionless model units, m.u.) across the line $z = z_0 + h_z$ with respect to the diffusive dissolution for different values of A_0. (For interpretation of the references to colour in this figure legend, the reader is referred to the web version of this article.)

a realistic theoretical model based on the Navier–Stokes equations. The integration of the nonlinear model reproduced well the dynamical behaviour of the experiments; in addition, the use of the measured parameters allowed for a semi-quantitative interpretation of the chemistry and physics at play in the explored systems. The model was also employed to decouple and study parametrically the relative influence of the main contributions to the flow (buoyancy- vs Marangoni-driven convection) through the characteristic numbers (R_i and M_i) directly linked to the experimental conditions (surfactant concentration, density of the DNAPL, etc.). To sum up, the proposed model catched all the essential features of the experimental systems and suggested criteria to optimise the interplay between buoyancy- and Marangoni-driven flows to enhance the DNAPL dissolution process. The model can be further refined to obtain more quantitative results by considering the complex nature of the microemulsion systems and by including cross-diffusion phenomena (Leaist and Hao, 1995; Vanag et al., 2008; Budroni et al., 2015a,b; Budroni, 2015).

The experimental model system we devised represents a proof of concept to demonstrate that the choice of a proper surfactant could help in designing more effective remediation strategies based on the co-solvent/surfactant flushing technology. Given the limitations of our lab-scale setup, it is difficult to give reliable values for the removal efficiency for in-field applications; however, we obtained an estimation of the DNAPL transfer rate to the water phase, by measuring the lowering of the liquid–liquid interface over time in the TCE/Syn 91/10 system. The analysis of the experimental frames yielded, for example, a velocity of transfer of 1.2×10^{-4} mm s^{-1} when [Syn 91/10] = 0.2 M, a value in line with that found for the mass transfer coefficient determined for spherical TCE droplets in surfactant solutions (Valletti et al., 2021). By considering a flat interface, the calculated transfer velocity would allow a theoretical removal rate of $\sim$ 10.5 L d^{-1} of DNAPL, in the case of a contact area of 1 m^2. If we take the TCE saturation concentration C_S^{TCE} = 0.64 M at [Syn 91/10] = 0.2 M (Table 3), we can roughly estimate a volume 1.8×10^4 L d^{-1} of the aqueous surfactant solution employed. To have a comparison, Brown et al. (1999) described a

3-day remediation process of a DNAPL contaminated aquifer, where $\sim$ 5000 L of a DNAPL were removed by employing 1.5×10^9 L of an aqueous solution with [SDS] = 0.26 M and [isopropanol] = 0.74 M. In another study, Jawitz and coworkers (Jawitz et al., 2000) reported a remediation case-study where $\sim$ 40 L of PCE were removed in 3 days by using $\sim$ 80000 L of 95% ethanol. In this study, we did not consider the effect of a water flow at the interface that would be present in real field applications for the delivery of the surfactant solution to the remediation spot. However, based on our results, we can say that the flow-rate of remediating solutions injected in flushing processes should be modulated to make the contact time between the aqueous and the DNAPL phases long enough to allow the onset of the fingering instabilities. Thus, the hydraulic residence time of the injected solution should be larger than the mixing time triggered by the hydrodynamic flows. In kinetic terms, the reciprocal of the residence time has to be of the order of 3.5 h^{-1}.

In conclusion, our results indicate that hydrodynamic instabilities can be successfully exploited, by selecting a suitable hydraulic residence time, to improve the removal rate of DNAPLs from aquifers and groundwater with a possible savings of additional compounds (surfactant and/or co-surfactants).

Declaration of competing interest

The authors declare that they have no known competing financial interests or personal relationships that could have appeared to influence the work reported in this paper.

Data availability

Data will be made available on request.

Acknowledgements

Appendix A. Supplementary data

Supplementary material related to this article can be found online at https://doi.org/10.1016/j.watres.2023.119608.

References

Acosta, E.J., Quraishi, S., 2014. Surfactant technologies for remediation of oil spills. In: Somasundaran, P., Patra, P., Farinato, R.S., Papadopoulos, K. (Eds.), Oil Spill Remediation. John Wiley & Sons, Inc, pp. 317–358. http://dx.doi.org/10.1002/9781118825662.ch15.

Agaoglu, B., Copty, N.K., Scheytt, T., Hinkelmann, R., 2015. Interphase mass transfer between fluids in subsurface formations: A review. Adv. Water Resour. 79, 162–194. http://dx.doi.org/10.1016/j.advwatres.2015.02.009.

Alizadeh, A., Nieto de Castro, C., Wakeham, W., 1980. The theory of the Taylor dispersion technique for liquid diffusivity measurements. Int. J. Thermophys. 1 (3), 243–284. http://dx.doi.org/10.1007/BF00517126.

Almarcha, C., R'Honi, Y., De Decker, Y., Trevelyan, P.M.J., Eckert, K., De Wit, A., 2011. Convective mixing induced by acid-base reactions. J. Phys. Chem. B 115 (32), 9739–9744. http://dx.doi.org/10.1021/jp202201e.

Apte, S., 2016. Selecting surfactants for the maximum inhibition of the activity of the multidrug resistance efflux pump transporter, P-glycoprotein: Conceptual development. J. Excip. Food Chem. 1 (3), 1133.

Bratsun, D.A., De Wit, A., 2004. On marangoni convective patterns driven by an exothermic chemical reaction in two-layer systems. Phys. Fluids 16 (4), 1082–1096. http://dx.doi.org/10.1063/1.1648641.

Brown, C.L., Delshad, M., Dwarakanath, V., Jackson, R.E., Londergan, J.T., Meinardus, H.W., McKinney, D.C., Oolman, T., Pope, G.A., Wade, W.H., 1999. Demonstration of surfactant flooding of an alluvial aquifer contaminated with dense nonaqueous phase liquid. In: Innovative Subsurface Remediation. In: ACS Symposium Series, vol. 725, American Chemical Society, pp. 64–85. http://dx.doi.org/10.1021/bk-1999-0725.ch006, Section: 6.

Broze, G., Zoller, U., 1999. Handbook of Detergents Part A. M. Dekker, New York; Basel, OCLC: 468456560.

Budroni, M.A., 2015. Cross-diffusion-driven hydrodynamic instabilities in a double-layer system: General classification and nonlinear simulations. Phys. Rev. E 92, 063007. http://dx.doi.org/10.1103/PhysRevE.92.063007, URL: https://link.aps.org/doi/10.1103/PhysRevE.92.063007.

Budroni, M.A., Carballido-Landeira, J., Intiso, A., Wit, A.D., Rossi, F., 2015a. Interfacial hydrodynamic instabilities driven by cross-diffusion in reverse microemulsions. Chaos 25 (6), 064502. http://dx.doi.org/10.1063/1.4922186.

Budroni, M.A., Lemaigre, L., De Wit, A., Rossi, F., 2015b. Cross-diffusion-induced convective patterns in microemulsion systems. Phys. Chem. Chem. Phys. 17 (3), 1593–1600. http://dx.doi.org/10.1039/C4CP02196G.

Budroni, M.A., Polo, A., Upadhyay, V., Bigaj, A., Rongy, L., 2021. Chemo-hydrodynamic pulsations in simple batch A + B → C systems. J. Chem. Phys. 154 (11), 114501. http://dx.doi.org/10.1063/5.0042560.

Budroni, M.A., Riolfo, L.A., Lemaigre, L., Rossi, F., Rustici, M., De Wit, A., 2014. Chemical control of hydrodynamic instabilities in partially miscible two-layer systems. J. Phys. Chem. Lett. 5 (5), 875–881. http://dx.doi.org/10.1021/jz5000403.

Budroni, M.A., Thomas, C., De Wit, A., 2017. Chemical control of dissolution-driven convection in partially miscible systems: nonlinear simulations and experiments. Phys. Chem. Chem. Phys. 19, 7936–7946. http://dx.doi.org/10.1039/C6CP08434F.

Callendar, R., Leaist, D.G., 2006. Diffusion coefficients for binary, ternary, and poly-disperse solutions from peak-width analysis of taylor dispersion profiles. J. Solut. Chem. 35 (3), 353–379.

Colombano, S., Davarzani, H., van Hullebusch, E.D., Huguenot, D., Guyonnet, D., Deparis, J., Lion, F., Ignatiadis, I., 2021. Comparison of thermal and chemical enhanced recovery of DNAPL in saturated porous media: 2D tank pumping experiments and two-phase flow modelling. Sci. Total Environ. 760, 143958. http://dx.doi.org/10.1016/j.scitotenv.2020.143958.

Cucciniello, R., Intiso, A., Castiglione, S., Genga, A., Proto, A., Rossi, F., 2017. Total oxidation of trichloroethylene over mayenite (Ca12Al14O33) catalyst. Appl. Catal. B 204, 167–172. http://dx.doi.org/10.1016/j.apcatb.2016.11.035.

De Wit, A., 2016. Chemo-hydrodynamic patterns in porous media. Phil. Trans. R. Soc. A 374 (2078), 20150419. http://dx.doi.org/10.1098/rsta.2015.0419, arXiv:https://royalsocietypublishing.org/doi/pdf/10.1098/rsta.2015.0419, URL: https://royalsocietypublishing.org/doi/abs/10.1098/rsta.2015.0419.

Ebrahimbabaie, P., Pichtel, J., 2021. Biotechnology and nanotechnology for remediation of chlorinated volatile organic compounds: Current perspectives. Environ. Sci. Pollut. Res. 28 (7), 7710–7741. http://dx.doi.org/10.1007/s11356-020-11598-y.

Engelmann, C., Händel, F., Binder, M., Yadav, P.K., Dietrich, P., Liedl, R., Walther, M., 2019. The fate of DNAPL contaminants in non-consolidated subsurface systems – discussion on the relevance of effective source zone geometries for plume propagation. J. Hard Mater. 375, 233–240. http://dx.doi.org/10.1016/j.jhazmat.2019.04.083.

Garza-Arévalo, J.I., Intiso, A., Proto, A., Rossi, F., Sanchez-Dominguez, M., 2019. Trichloroethylene solubilization using a series of commercial biodegradable ethoxylated fatty alcohol surfactants. J. Chem. Technol. Biotechnol. 94 (11), 3523–3529. http://dx.doi.org/10.1002/jctb.5965.

Harendra, S., Vipulanandan, C., 2011. Effects of surfactants on solubilization of perchloroethylene (PCE) and trichloroethylene (TCE). Ind. Eng. Chem. Res. 50 (9), 5831–5837. http://dx.doi.org/10.1021/ie102589e.

Huo, L., Liu, G., Yang, X., Ahmad, Z., Zhong, H., 2020. Surfactant-enhanced aquifer remediation: mechanisms, influences, limitations and the countermeasures. Chemosphere 252, 126620. http://dx.doi.org/10.1016/j.chemosphere.2020.126620.

Hussain, A., Rehman, F., Rafeeq, H., Waqas, M., Asghar, A., Afsheen, N., Rahdar, A., Bilal, M., Iqbal, H.M.N., 2022. In-situ, Ex-situ, and nano-remediation strategies to treat polluted soil, water, and air – A review. Chemosphere 289, 133252. http://dx.doi.org/10.1016/j.chemosphere.2021.133252.

Intiso, A., Martinez-Triguero, J., Cucciniello, R., Rossi, F., Palomares, A.E., 2019. Influence of the synthesis method on the catalytic activity of mayenite for the oxidation of gas-phase trichloroethylene. Sci. Rep. 9 (1), 425. http://dx.doi.org/10.1038/s41598-018-36708-2.

Intiso, A., Miele, Y., Marchettini, N., Proto, A., Sánchez-Domínguez, M., Rossi, F., 2018. Enhanced solubility of trichloroethylene (TCE) by a poly-oxyethylene alcohol as green surfactant. Environ. Technol. Innov. 12, 72–79. http://dx.doi.org/10.1016/j.eti.2018.08.001.

Jawitz, J.W., Sillan, R.K., Annable, M.D., Rao, P.S.C., Warner, K., 2000. In-situ alcohol flushing of a DNAPL source zone at a dry cleaner site. Environ. Sci. Technol. 34 (17), 3722–3729. http://dx.doi.org/10.1021/es9913737.

Joannes, L., Dubois, F., Legros, J.-C., 2003. Phase-shifting schlieren: High-resolution quantitative schlieren that uses the phase-shifting technique principle. Appl. Opt. 42 (25), 5046–5053. http://dx.doi.org/10.1364/AO.42.005046.

Jotkar, M., De Wit, A., Rongy, L., 2019. Enhanced convective dissolution due to an A + B=C reaction: control of the non-linear dynamics via solutal density contributions. Phys. Chem. Chem. Phys. 21, 6432–6442. http://dx.doi.org/10.1039/C8CP07642A.

Kang, S., Lim, H.S., Gao, Y., Kang, J., Jeong, H.Y., 2019. Evaluation of ethoxylated nonionic surfactants for solubilization of chlorinated organic phases: effects of partitioning loss and macroemulsion formation. J. Contam. Hydrol. 223, 103475. http://dx.doi.org/10.1016/j.jconhyd.2019.03.007.

Kibbey, T.C.G., Ramsburg, C.A., Pennell, K.D., Hayes, K.F., 2002. Implications of alcohol partitioning behavior for in situ density modification of entrapped dense nonaqueous phase liquids. Environ. Sci. Technol. 36 (1), 104–111. http://dx.doi.org/10.1021/es010966q.

Lagzi, I., 2015. Self-division of a mineral oil fatty acid droplet. Chem. Phys. Lett. 640, 1–4. http://dx.doi.org/10.1016/j.cplett.2015.09.053.

Lappa, M., Piccolo, C., Carotenuto, L., 2005. Fluid dynamics and dissolution kinetics in immiscible organic systems with dispersed droplets. Colloids Surf. A 261 (1), 177–186. http://dx.doi.org/10.1016/j.colsurfa.2004.11.042, A collection of papers presented at the International Workshop on Bubble and Drop Interfaces 2004, Genoa (Italy), 25th-28th April, 2004.

Leaist, D., Hao, L., 1995. Size distribution model for chemical interdiffusion in water aot heptane water-in-oil microemulsions. J. Phys. Chem. 99 (34), 12896–12901.

Lemaigre, L., Budroni, M.A., Riolfo, L.A., Grosfils, P., De Wit, A., 2013. Asymmetric Rayleigh-taylor and double-diffusive fingers in reactive systems. Phys. Fluids 25 (1), 014103. http://dx.doi.org/10.1063/1.4774321.

Levenberg, K., 1944. A method for the solution of certain non-linear problems in least squares. Quart. Appl. Math. 2 (2), 164–168. http://dx.doi.org/10.1090/qam/10666.

Liu, Y., Illangasekare, T.H., Kitanidis, P.K., 2014. Long-term mass transfer and mixing-controlled reactions of a DNAPL plume from persistent residuals. J. Contam. Hydrol. 157, 11–24. http://dx.doi.org/10.1016/j.jconhyd.2013.10.008.

Loodts, V., Thomas, C., Rongy, L., De Wit, A., 2014. Control of convective dissolution by chemical reactions: General classification and application to CO2 dissolution in reactive aqueous solutions. Phys. Rev. Lett. 113, 114501.

Luciano, A., Mancini, G., Torretta, V., Viotti, P., 2018. An empirical model for the evaluation of the dissolution rate from a DNAPL-contaminated area. Environ. Sci. Pollut. Res. 25 (34), 33992–34004. http://dx.doi.org/10.1007/s11356-018-3193-6.

Luciano, A., Viotti, P., Papini, M.P., 2010. Laboratory investigation of DNAPL migration in porous media. J. Hard Mater. 176 (1), 1006–1017. http://dx.doi.org/10.1016/j.jhazmat.2009.11.141.

Luciano, A., Viotti, P., Papini, M.P., 2012. On morphometric properties of DNAPL sources: relating architecture to mass reduction. Water Air Soil Pollut. 223 (5), 2849–2864. http://dx.doi.org/10.1007/s11270-011-1071-7.

Mao, X., Jiang, R., Xiao, W., Yu, J., 2015. Use of surfactants for the remediation of contaminated soils: a review. J. Hard Mater. 285, 419–435.

Marquardt, D.W., 1963. An algorithm for least-squares estimation of nonlinear parameters. J. Soc. Ind. Appl. Math. 11 (2), 431–441. http://dx.doi.org/10.1137/0111030.

Moccia, E., Intiso, A., Cicatelli, A., Proto, A., Guarino, F., Iannece, P., Castiglione, S., Rossi, F., 2017. Use of Zea mays L. in phytoremediation of trichloroethylene. Environ. Sci. Pollut. Res. 24, 11053–11060. http://dx.doi.org/10.1007/s11356-016-7570-8.

Peaceman, D.W., Rachford, H.H., 1955. The numerical solution of parabolic and elliptic differential equations. J. Soc. Ind. Appl. Math. 3, 28.

Ramsburg, C.A., Pennell, K.D., 2002. Density-modified displacement for DNAPL source zone remediation: density conversion and recovery in heterogeneous aquifer cells. Environ. Sci. Technol. 36 (14), 3176–3187. http://dx.doi.org/10.1021/es011403h.

Rossi, F., Cucciniello, R., Intiso, A., Proto, A., Motta, O., Marchettini, N., 2015. Determination of the trichloroethylene diffusion coefficient in water. AIChE J. 61 (10), 3511–3515. http://dx.doi.org/10.1002/aic.14861.

Rossi, F., Vanag, V.K., Epstein, I.R., 2011. Pentanary cross-diffusion in water-in-oil microemulsions loaded with two components of the Belousov-Zhabotinsky reaction. Chem. Eur. J. 17 (7), 2138–2145. http://dx.doi.org/10.1002/chem.201002069.

Rossi, F., Vanag, V.K., Tiezzi, E., Epstein, I.R., 2010. Quaternary cross-diffusion in water-in-oil microemulsions loaded with a component of the Belousov-Zhabotinsky reaction. J. Phys. Chem. B 114 (24), 8140–8146. http://dx.doi.org/10.1021/jp102753b.

Rossi, F., Varsalona, R., Turco Liveri, M.L., 2008. New features in the dynamics of a ferroin-catalyzed Belousov–Zhabotinsky reaction induced by a zwitterionic surfactant. Chem. Phys. Lett. 463 (4), 378–382. http://dx.doi.org/10.1016/j.cplett.2008.08.082.

Saffman, P.G., Taylor, G.I., 1958. The penetration of a fluid into a porous medium or Hele-Shaw cell containing a more viscous liquid. Proc. R. Soc. Lond. Ser. A Math. Phys. Sci. 245 (1242), 312–329. http://dx.doi.org/10.1098/rspa.1958.0085.

Schneider, C.A., Rasband, W.S., Eliceiri, K.W., 2012. NIH Image to ImageJ: 25 years of image analysis. Nature Methods 9 (7), 671–675.

Sternling, C.V., Scriven, L.E., 1959. Interfacial turbulence: Hydrodynamic instability and the marangoni effect. AIChE J. 5 (4), 514–523. http://dx.doi.org/10.1002/aic.690050421.

Taylor, G., 1953. Dispersion of soluble matter in solvent flowing slowly through a tube. Proc. R. Soc. Lond. A Math. Phys. Eng. Sci. 219 (1137), 186–203. http://dx.doi.org/10.1098/rspa.1953.0139.

Trevelian, P.M.J., Almarcha, C., De Wit, A., 2011. Buoyancy-driven instabilities of miscible two-layer stratifications in porous media and Hele-Shaw cells. J. Fluid Mech. 670, 38–65. http://dx.doi.org/10.1017/S0022112010005008.

Trevelyan, P.M., Almarcha, C., De Wit, A., 2011. Buoyancy-driven instabilities of miscible two-layer stratifications in porous media and Hele-Shaw cells. J. Fluid Mech. 670, 38–65. http://dx.doi.org/10.1017/S0022112010005008.

Valletti, N., Acar, M., Cucciniello, R., Magrini, C., Budroni, M.A., Tatini, D., Proto, A., Marchettini, N., Lo Nostro, P., Rossi, F., 2022. Glycerol carbonate structuring in aqueous solutions as inferred from mutual diffusion coefficient, density and viscosity measurements in the temperature range 283.15–313.15 K. J. Mol. Liq. 357, 119114. http://dx.doi.org/10.1016/j.molliq.2022.119114.

Valletti, N., Budroni, M.A., Lagzi, I., Marchettini, N., Sanchez-Dominguez, M., Rossi, F., 2021. Interfacial mass transfer in trichloroethylene/surfactants/ water systems: Implications for remediation strategies. Reactions 2 (3), 312–322. http://dx.doi.org/10.3390/reactions2030020.

Vanag, V.K., Rossi, F., Cherkashin, A., Epstein, I.R., 2008. Cross-diffusion in a water-in-oil microemulsion loaded with malonic acid or ferroin. taylor dispersion method for four-component systems. J. Phys. Chem. B 112 (30), 9058–9070.

Wang, X., Ren, L., Long, T., Geng, C., Tian, X., 2022. Migration and remediation of organic liquid pollutants in porous soils and sedimentary rocks: A review. Environ. Chem. Lett. http://dx.doi.org/10.1007/s10311-022-01506-w.

Yang, C., Liu, F., Zhang, C., Offiong, N.-A., Dong, J., 2022. Density-modification displacement using colloidal biliquid aphron for entrapped DNAPL contaminated aquifer remediation. J. Hard Mater. 432, 128641. http://dx.doi.org/10.1016/j.jhazmat.2022.128641.

Zhu, Y., Free, M.L., 2015. Experimental investigation and modeling of the performance of pure and mixed surfactant inhibitors: partitioning and distribution in water-oil environments. J. Electrochem. Soc. 162 (14), C702–C717. http://dx.doi.org/10.1149/2.0291514jes.

Zimmerman, J.B., Kibbey, T.C.G., Cowell, M.A., Hayes, K.F., 1999. Partitioning of ethoxylated nonionic surfactants into nonaqueous-phase organic liquids: influence on solubilization behavior. Environ. Sci. Technol. 33 (1), 169–176. http://dx.doi.org/10.1021/es9802910.